RESEARCH ARTICLE

Valley-polarized quantum anomalous Hall effect in van der Waals heterostructures based on monolayer jacutingaite family materials

Xudong Zhu[1,2,*], Yuqian Chen[1,2,*], Zheng Liu[1,2,†], Yulei Han[3,‡], Zhenhua Qiao[1,2,§]

[1] ICQD, Hefei National Research Center for Physical Sciences at the Microscale, University of Science and Technology of China, Hefei 230026, China
[2] CAS Key Laboratory of Strongly-Coupled Quantum Matter Physics, and Department of Physics, University of Science and Technology of China, Hefei 230026, China
[3] Department of Physics, Fuzhou University, Fuzhou 350108, China
Corresponding authors. E-mail: [†]zhengliu@mail.ustc.edu.cn, [‡]han@fzu.edu.cn, [§]qiao@ustc.edu.cn
[*]These authors contributted equally to this work.

Supporting Information

Contents

I. COMPUTATIONAL DETAILS

A.   First-principles calculation with GGA+U method

Our first-principles calculations were performed by using the projected augmented-wave method [1] as implemented in the Vienna *ab initio* simulation package (VASP) [2, 3]. The generalized gradient approximation of the Perdew-Burke-Ernzerhof (PBE) type was used to describe the exchange-correlation interaction [4]. The vdW interaction was treated by using DFT-D3 functional [5]. All atoms were fully relaxed until the energy (10^{-6} eV) and the Hellmann-Feynman force (0.01 eV/Å) convergence thresholds were reached. A vacuum buffer layer of 20 Å was used to avoid unnecessary interaction along z direction between adjacent slabs. The plane-wave energy cutoff was set to be 520 eV. The Γ-centered Monkhorst-Pack k-point grid of $11 \times 11 \times 1$ was adopted in all our calculations.

To deal with the strong correlation effect of $3d$ magnetic elements in our first-principles calculation (Fe, Co, Ni, Cr, V, and Mn), the GGA+U method [6] was used with the corresponding on-site repulsion energy U and exchange interaction J [15–19] as described in Table S1. It is noteworthy that GGA+U method was used in all calculations including structural optimization. Two-dimensional magnets MY_2 (M = Fe, Co, Ni; Y = Cl, Br, I), CI_3, VI_3, and $MnBi_2Te_4$ are ferromagnetic [11–22]. One can manipulate the easy magnetization axis of two-dimensional ferromagnets to be out-of-plane by electric field, low-density magnetic field, and strain [22–26]. Therefore, we set the magnetic moments to be parallel to z direction in our calculation.

TABLE S1. On-site repulsion energies U, exchange parameters J and corresponding references.

Element	U (eV)	J (eV)	U_{eff} (eV)	Reference
Co	3.67	0.00	3.67	Lv et *al.* [16]
Cr	3.00	0.87	2.13	Tian et *al.* [15]
V	3.68	0.00	3.68	Tian et *al.* [15]
Fe	4.00	0.80	3.20	Botana et *al.* [17]
Ni	4.00	0.80	3.20	Botana et *al.* [17]
Mn	5.34	0.00	5.34	Otrokov et *al.* [18]

B. Projected orbital contributions and Wannier functions

Before carrying out the maximally-localized Wannier functions, we calculated the orbital-projected band structures of all systems. Here, we take the $Pt_2HgSe_3/NiBr_2$ heterostructure as an example and the corresponding projected orbital contributions are demonstrated in Fig. S1. One can observe that Pt-d, Hg-s, Se-p, Ni-d, and Br-p mostly contribute to the energy bands near Fermi level, supporting the following projection of Wannier functions.
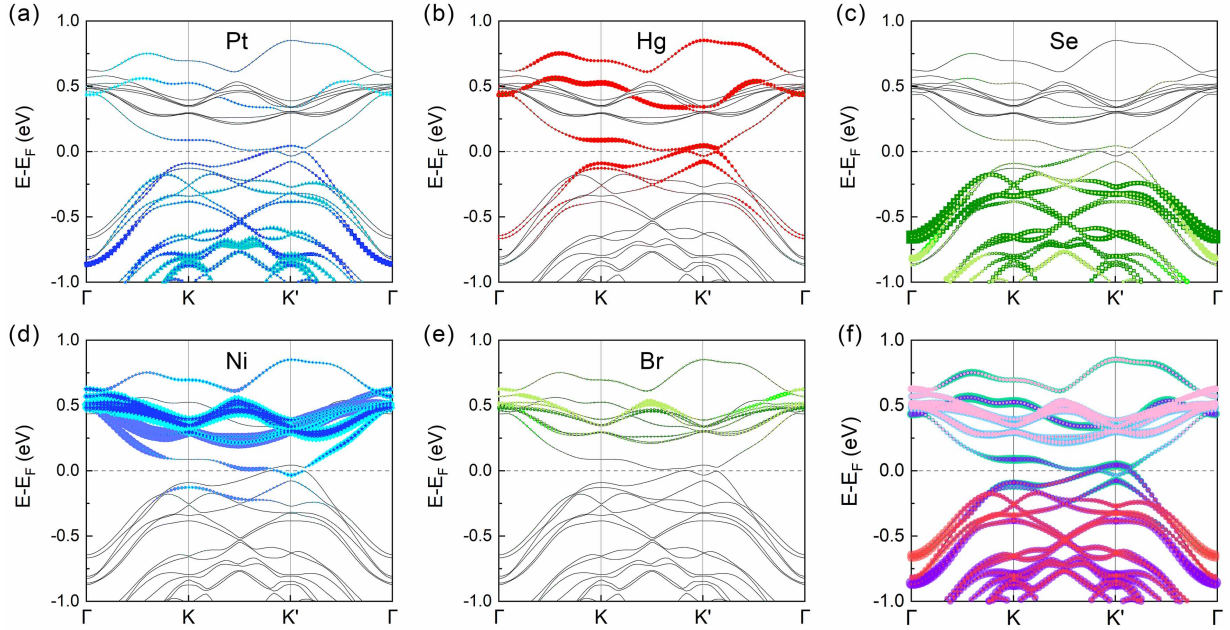

FIG. S1. The projected orbital contributions of $Pt_2HgSe_3/NiBr_2$ vdW heterostructure with spin-orbit coupling. Red, blue and green dots represent the contribution of s, p and d orbitals from (a) Pt, (b) Hg, (c) Se, (d) Ni and (e) Br elements, respectively. (f) displays the mostly contributed orbitals as Pt-d, Hg-s, Se-p, Ni-d, and Br-p in purple, green, red, blue, and pink, respectively.

Therefore, we obtained the Bloch wave functions of Pt-d, Hg-s, Se-p, Ni-d, and Br-p orbitals from our first-principles calculation and projected them on Wannier basises by using maximally-localized Wannier functions as implemented in Wannier90 software package [27, 28]. Subsequently, we carried out the fitting band structures as plotted in Fig. S2. One can find that the band structures fitted by using maximally-localized Wannier functions agree well with the first-principles calculation result, implying that we have obtained a set of Wannier basis with fine fitness.
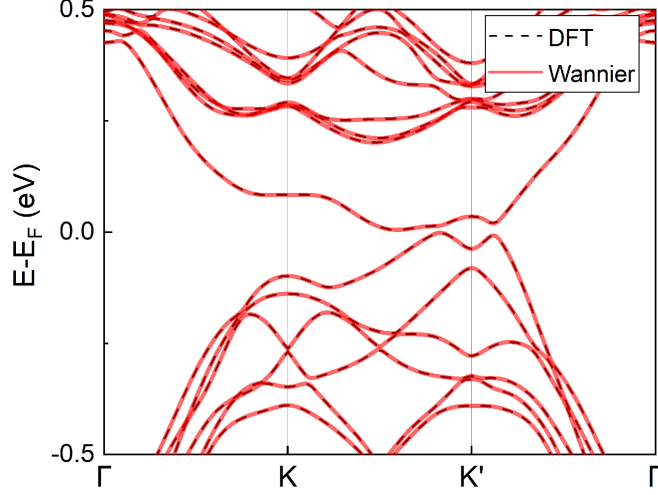
FIG. S2. Band structures of the $Pt_2HgSe_3/NiBr_2$ heterostructure plotted by using maximally-localized Wannier functions versus by using first-principles calculations method.

C. Topological properties calculation method

Topological properties were carried out by using maximally-localized Wannier functions as implemented in Wannier90 and WannierTools software packages [27–29].

Berry curvature of the n-th band at momentum $\boldsymbol{k}$ is calculated by

$$\Omega_n(\boldsymbol{k}) = 2\mathrm{Im} \sum_{m \neq n} \frac{\langle u_n(\boldsymbol{k})|\nabla_{\boldsymbol{k}} H(\boldsymbol{k})|u_m(\boldsymbol{k})\rangle \times \langle u_m(\boldsymbol{k})|\nabla_{\boldsymbol{k}} H(\boldsymbol{k})|u_n(\boldsymbol{k})\rangle}{(\epsilon_{n,\boldsymbol{k}} - \epsilon_{m,\boldsymbol{k}})^2} \ , \tag{1}$$

where $\epsilon_{n,\boldsymbol{k}}$ is the electronic band structure.

Chern number of the n-th band is calculated by

$$\mathcal{C} = \frac{1}{2\pi} \int_{\mathrm{BZ}} \mathrm{d}^2\boldsymbol{k} \, \Omega_n(\boldsymbol{k}) \ , \tag{2}$$

where the integration run over the states at momentum $\boldsymbol{k}$ in n-th band in first Brillouin zone below the Fermi energy.

Anomalous Hall conductance is calculated by

$$\sigma_{xy} = \frac{e^2}{\hbar} \frac{1}{2\pi} \int_{\mathrm{BZ}} \mathrm{d}^2\boldsymbol{k} \, \Omega_n(\boldsymbol{k}) \ , \tag{3}$$

i.e., $\sigma_{xy} = \mathcal{C}e^2/\hbar$.

II. MAGNETIC PROPERTIES OF TWO-DIMENSIONAL FERROMAGNETIC SUBSTRATES

In this work, monolayer metal dihalides MY_2 (M = Fe, Co, Ni; Y = Cl, Br, I) and two-dimensional magnets CI_3, VI_3, and $MnBi_2Te_4$ are used to induce magnetic exchange interactions [11–21]. These two-dimensional magnets have been proved that they all possess the ferromagnetic (FM) ground state at 0 K in freestanding monolayer. Additionally, they are also energetically and dynamically stable in monolayer. The Curie temperatures and dynamical stabilities of the ferromagnetic substrates and whether they are already synthesized in experiments are all summarized in Table S2. The band gap of every material and their band alignment are shown in the band edges as plotted in Fig. 2. Although the monolayer metal dihalides MY_2 have not been synthesized yet, the bulk single crystals are all synthesized and they are reported to be cleaved easily to monolayer due to their layered crystal structures [11–15].

TABLE S2. Curie temperatures T_c, structural stability of two-dimensional monolayer ferromagnetic substrates, and whether they are already synthesized in experiments and corresponding references. ML denotes as "monolayer" while SL denotes as "septuple layer".

FM Substrate	T_c (K)	Stability	Synthesis	Reference
$FeCl_2$	109	Yes	Bulk	[11, 12]
$FeBr_2$	81	Yes	Bulk	[11, 12]
FeI_2	42	Yes	Bulk	[11, 12]
$CoCl_2$	85	Yes	Bulk	[11, 12]
CoBr2	23	Yes	Bulk	[11, 12]
$NiCl_2$	138	Yes	Bulk	[11, 12]
$NiBr_2$	132	Yes	Bulk	[11, 12]
NiI_2	129	Yes	Bulk	[11, 12]
CrI_3	45	Yes	Bulk, ML	[13]
VI_3	98	Yes	Bulk, ML	[15]
$MnBi_2Te_4$ (1SL)	12	Yes	Bulk, ML	[14]

III. LATTICE MISMATCH FOR ALL PT$_2AX_3$/FERROMAGNETIC SUBSTRATE HETEROSTRUCTURES

In our calculation, monolayer jacutingaite family materials and monolayer ferromagnetic substrates were fully relaxed with GGA+U method. The optimized lattice constants were summarized in Table S3, respectively.

Subsequently, we investigate the lattice mismatch between 1×1 Pt$_2AX_3$ and different ferromagnetic substrates to construct a van der Waals (vdW) heterostructure. The lattice mismatch δ can be defined as

$$\delta = \frac{2(a_{\mathrm{jac}} - a_{\mathrm{sub}})}{a_{\mathrm{jac}} + a_{\mathrm{sub}}} \times 100 \ \% \ , \tag{4}$$

where a_{jac} denotes the lattice constant of 1×1 Pt$_2AX_3$ and a_{sub} denotes the lattice constant of ferromagnetic substrate with respective supercell size. We summarized the lattice mismatch for every possible vdW heterostructure combination in Table S3.

In Table S3, one can see that the highlighted systems exhibit well-matched lattice constants, such as 1×1 Pt$_2$CdS$_3$/2×2 CoCl$_2$ exhibits negligible lattice mismatch of only 0.0210 %, indicating that they can finely form a two-dimensional vdW heterostructure. However, some systems are demonstrated to be difficult to match with each other. For example, the lattice mismatch of 1×1 Pt$_2$ZnTe$_3$/$\sqrt{3} \times \sqrt{3}$ NiI$_2$ reaches up to 13.0225 %, leading to an unstable atomic structure.

Considering the experimental feasibility, we selected the vdW heterostructure whose lattice mismatch is smaller than 5 % to perform further calculations and highlighted these 62 kinds of lattice-matched systems in Table S3.

TABLE S3. Lattice constants (Å), and lattice mismatch (%) with corresponding substrate supercell for Pt$_2$AX$_3$/ferromagnetic substrate heterostructures (A = Hg, Cd, Zn; X = S, Se, Te). Pt$_2$AX$_3$ is considered as 1×1 unit cell. Systems with over 5 % lattice mismatch are excluded in following calculations due to the lack of implementation possibility in experiments. Highlighted systems are screen out to further explore physical properties.

FM Substrate	Supercell Size	Lattice Const. (Å)	Pt$_2$HgS$_3$ 7.1620	Pt$_2$HgSe$_3$ 7.4398	Pt$_2$HgTe$_3$ 7.8568	Pt$_2$CdS$_3$ 7.1462	Pt$_2$CdSe$_3$ 7.4286	Pt$_2$CdTe$_3$ 7.8503	Pt$_2$ZnS$_3$ 7.1306	Pt$_2$ZnSe$_3$ 7.4002	Pt$_2$ZnTe$_3$ 7.8053
FeCl$_2$	2×2	3.5680	**0.3625**	**4.1668**	9.6134	**0.1415**	**4.0166**	9.5313	**-0.0776**	**3.6341**	8.9574
FeBr$_2$	2×2	3.7610	**4.9038**	**-1.0999**	**4.3527**	-5.1247	**-1.2502**	**4.2705**	-5.3437	**-1.6328**	**3.6955**
FeI2	2×2	4.0415	12.0830	-8.2880	**-2.8392**	-12.3032	-8.4381	**-2.9214**	-12.5215	-8.8199	**-3.4965**
NiCl$_2$	2×2	3.4830	**2.7720**	6.5747	12.0159	**2.5510**	6.4245	11.9340	**2.3319**	6.0423	11.3607
NiBr$_2$	2×2	3.6778	**2.6690**	**1.1356**	6.5866	**-2.8900**	**0.9853**	6.5045	**-3.1091**	**0.6027**	5.9298
NiI2	2×2	3.9554	-9.9358	-6.1371	**-0.6857**	-10.1563	-6.2873	**-0.7679**	-10.3748	-6.6695	**-1.3431**
CoCl$_2$	2×2	3.5723	**0.2421**	**4.0464**	9.4932	**0.0210**	**3.8962**	9.4111	**-0.1980**	**3.5137**	8.8371
CoBr$_2$	2×2	3.7659	**-5.0340**	**-1.2302**	**4.2224**	-5.2549	**-1.3805**	**4.1402**	-5.4739	**-1.7631**	**3.5653**
CrI$_3$	1×1	6.9597	**2.8643**	6.6669	12.1079	**2.6433**	6.5168	12.0260	**2.4242**	6.1345	11.4528
VI$_3$	1×1	7.0761	**1.2061**	**5.0099**	10.4548	**0.9851**	**4.8597**	10.3728	**0.7659**	**4.4773**	9.7991
FeI$_2$	$\sqrt{3} \times \sqrt{3}$	4.0415	**2.2863**	6.0894	11.5318	**2.0653**	5.9392	11.4498	**1.8461**	5.5569	10.8765
NiI$_2$	$\sqrt{3} \times \sqrt{3}$	3.9554	**4.4393**	8.2403	13.6769	**4.2184**	8.0902	13.5951	**3.9994**	7.7082	13.0225
MnBi$_2$Te$_4$	$\sqrt{3} \times \sqrt{3}$	4.3543	-5.1668	**-1.3630**	**4.0897**	-5.3876	**-1.5133**	**4.0075**	-5.6066	**-1.8959**	**3.4325**

IV. SCHEMATIC OF FOUR TYPES OF VDW HETEROSTRUCTURE STACKING ORDERS

Different stacking orders were also considered. We adopt four kinds of stacking orders as shown in Fig.S3. According to the atom site directly below the $A1$ site, they can be classified to (i) M, (ii) $Y(\text{top})$, (iii) $Y(\text{hollow})$, and (iv) $MY(\text{bridge})$, respectively. We calculated the total energy of different configurations for every well-matched system and finally find the most stable stacking order as listed in Table S5.
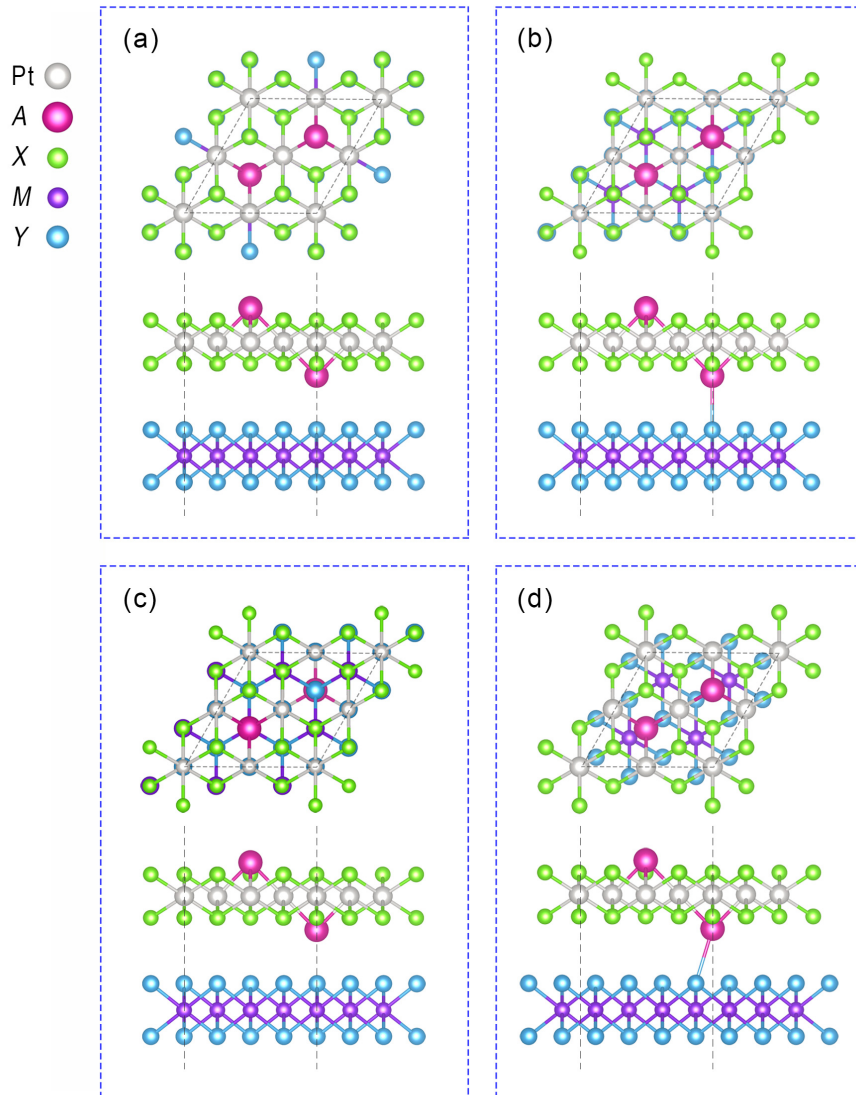

FIG. S3. Top and side views of four different types of stacking configurations of the Pt_2AX_3/MY_2 heterostructure: (a) M, (b) $Y(\text{top})$, (c) $Y(\text{hollow})$, and (d) $MY(\text{bridge})$.

V. MOLECULAR DYNAMICS SIMULATIONS FOR 4 NON-TRIVIAL SYSTEMS

To verify the structural stability of 4 representative valley-polarized QAHE systems among the 44 kinds of valley polarization heterostructures (Pt_2HgSe_3/$NiBr_2$, Pt_2ZnS_3/$CoBr_2$, Pt_2HgS_3/$NiBr_2$, and Pt_2HgSe_3/$CoBr_2$), we perform *ab initio* molecular dynamics (MD) simulations as implemented in VASP. The canonical ensemble (NVT) was adopted for the simulations by using Nose thermostat. The molecular dynamics simulations are performed by using 3×3 supercell of Pt_2HgSe_3/$NiBr_2$, Pt_2ZnS_3/$CoBr_2$, Pt_2HgS_3/$NiBr_2$, and Pt_2HgSe_3/$CoBr_2$ heterostructures (216 atoms) with the temperature of 300 K and the time step of 1 fs. After 5000 steps (5 ps) simulations, the 4 representative heterostructures preserve their respective structures as shown in Figs. S4-S7, indicating the structural stability of 4 non-trivial heterostructures.
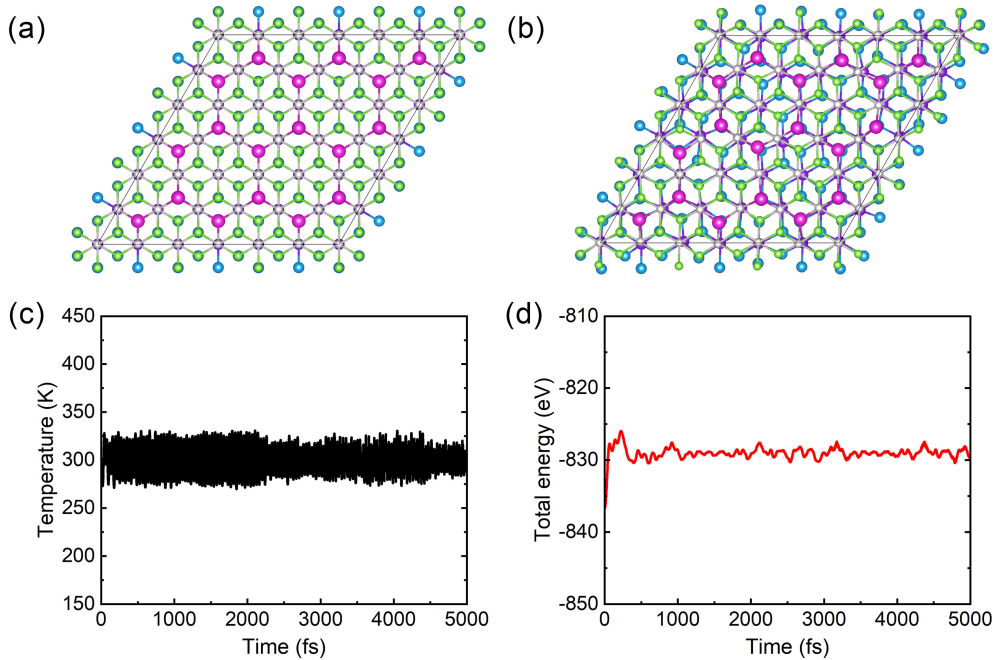
FIG. S4. The *ab initio* molecular dynamics simulations of Pt_2HgSe_3/$NiBr_2$ heterostructure. (a) The initial structure and the (b) final structure after 5 ps of MD simulations. The evolution of (c) the temperature and (d) total energy during MD simulations.
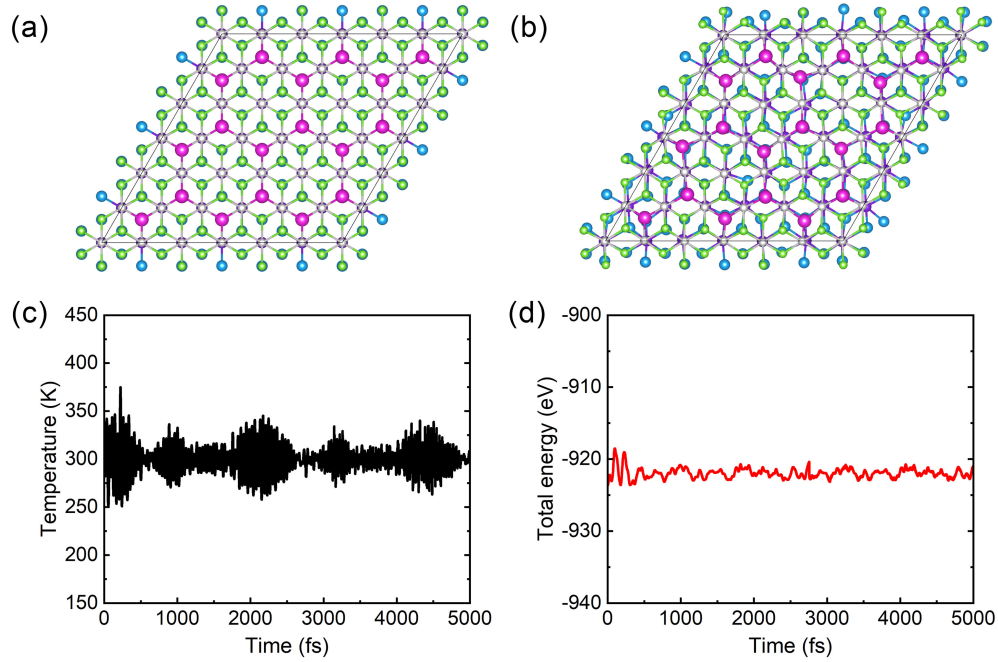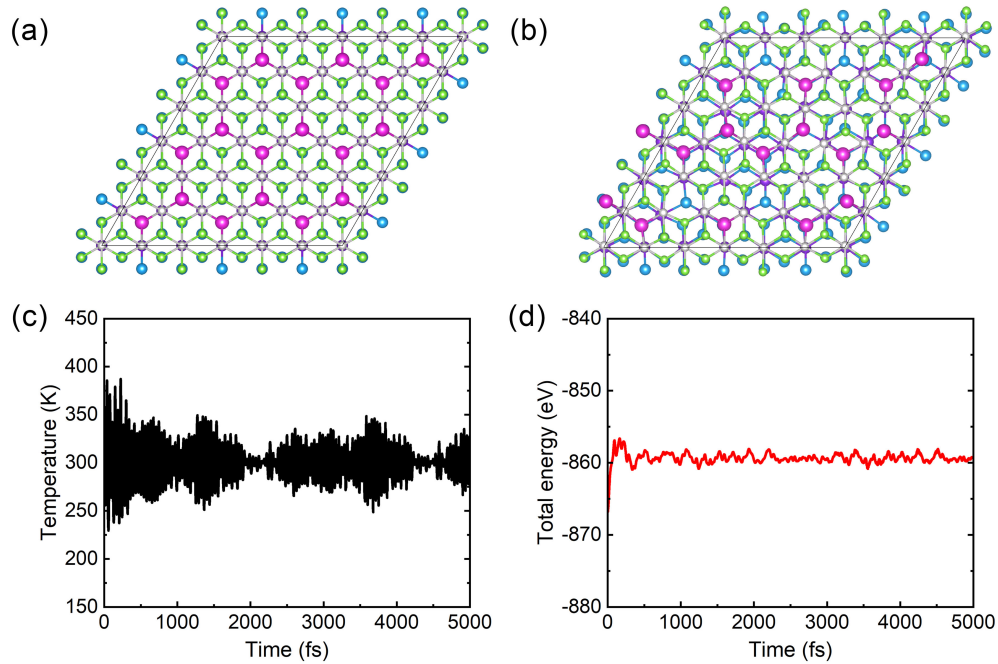
10

FIG. S5. The *ab initio* molecular dynamics simulations of $Pt_2ZnS_3/CoBr_2$ heterostructure. (a) The initial structure and the (b) final structure after 5 ps of MD simulations. The evolution of (c) the temperature and (d) total energy during MD simulations.
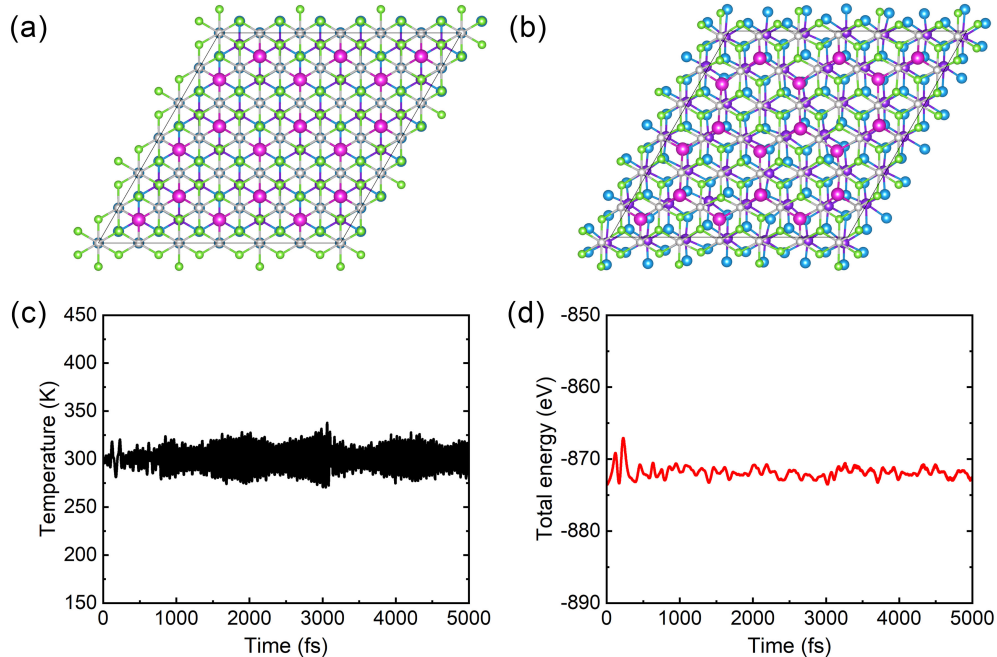

FIG. S6. The *ab initio* molecular dynamics simulations of $Pt_2HgS_3/NiBr_2$ heterostructure. (a) The initial structure and the (b) final structure after 5 ps of MD simulations. The evolution of (c) the temperature and (d) total energy during MD simulations.

11

FIG. S7. The *ab initio* molecular dynamics simulations of $Pt_2HgSe_3/CoBr_2$ heterostructure. (a) The initial structure and the (b) final structure after 5 ps of MD simulations. The evolution of (c) the temperature and (d) total energy during MD simulations.

VI.   MAGNETIC EXCHANGE INTERACTION BETWEEN FERROMAGNETIC SUBSTRATES AND MONOLAYER JACUTINGAITE FAMILY MATERIALS

A.   Magnetic properties of $CoBr_2$ coupling to Pt_2HgSe_3 and Pt_2ZnS_3

To obtain the influence of Pt_2HgSe_3 or Pt_2ZnS_3 monolayer on the magnetic properties of $CoBr_2$, we systematically calculated the ferromagnetic properties and magnetocrystalline anisotropy energy of freestanding $CoBr_2$, $Pt_2HgSe_3/CoBr_2$, and $Pt_2ZnS_3/CoBr_2$. As shown in Table R1, the energy differences between ferromagnetic and antiferromagnetic states $\Delta E = E_{FM} - E_{AFM}$ are all negative value, demonstrating that the ferromagnetic ground state of $CoBr_2$ is very stable. Detailed analyses show that ferromagnetism of $CoBr_2$ is obviously enhanced in $Pt_2ZnS_3/CoBr_2$ heterostructure while slightly weakened in $Pt_2HgSe_3/CoBr_2$ heterostructure. Given the ferromagnetic ground states of freestanding $CoBr_2$, $Pt_2HgSe_3/CoBr_2$, and $Pt_2ZnS_3/CoBr_2$, we also calculate the magnetocrystalline anisotropy energy (MAE) of monolayer $CoBr_2$ with and without Pt_2HgSe_3 or Pt_2ZnS_3 mono-

12

layer. The MAE is defined as the energy difference between in-plane and out-of-plane magnetization, i.e., $MAE = E_{\text{in-plane}} - E_{\text{out-of-plane}}$. The calculated results show that the MAE is -0.026 meV/Co for freestanding $CoBr_2$ and -0.024 meV/Co for $Pt_2HgSe_3/CoBr_2$ heterostructure. The Pt_2HgSe_3 layer has little influence on the MAE of $CoBr_2$. Note that, the MAE in $Pt_2HgSe_3/CoBr_2$ heterostructure is very small (on the order of 10^{-2} meV), which indicates that the direction of magnetic moments can be easily tuned to z direction by using a weak external magnetic field. It is worth mentioning that the MAE of $Pt_2ZnS_3/CoBr_2$ heterostructure is 1.795 meV/Co, suggesting that the magnetic easy axis of $CoBr_2$ can be tuned by Pt_2ZnS_3 from in-plane to out-of-plane direction, which is beneficial to the experimental realization of valley-polarized QAHE.

TABLE S4. Magnetic properties of CoB_2 monolayer with and without Pt_2HgSe_3 and Pt_2ZnS_3.

	CoB_2	Pt_2HgSe_3/CoB_2	Pt_2ZnS_3/CoB_2
$E_{\text{FM}} - E_{\text{AFM}}$ (meV/Co)	-2.834	-2.782	-5.112
MAE (meV/Co)	-0.026	-0.024	1.795

B. Magnetic proximity effect induced by ferromagnetic substrates

Considering the importance of the magnetic proximity effect to 2D ferromagnetic heterostructures, we calculate the band structures of $Pt_2HgSe_3/NiBr_2$, $Pt_2ZnS_3/CoBr_2$, $Pt_2HgS_3/NiBr_2$, and $Pt_2HgSe_3/CoBr_2$ without and with magnetization to illustrate the effect of magnetic exchange interaction of ferromagnetic substrates. As shown in Fig. S8, we can notice that the shapes of the band structures without and with magnetization are similar except for the bands near the Fermi level. When the magnetism of the ferromagnetic substrates is considered, one can find that the large spin splitting appears near the Fermi level in the spin-polarized band structures of every system, which is induced by the magnetic proximity effect of the ferromagnetic substrates. Furthermore, the band structures of the Pt_2AX_3 near the Fermi level are also modified by the magnetic exchange interaction at the interface. So, when SOC is further considered, both the time-reversal and inversion symmetries are broken, leading to the non-trivial band gaps as plotted in Fig. 4.
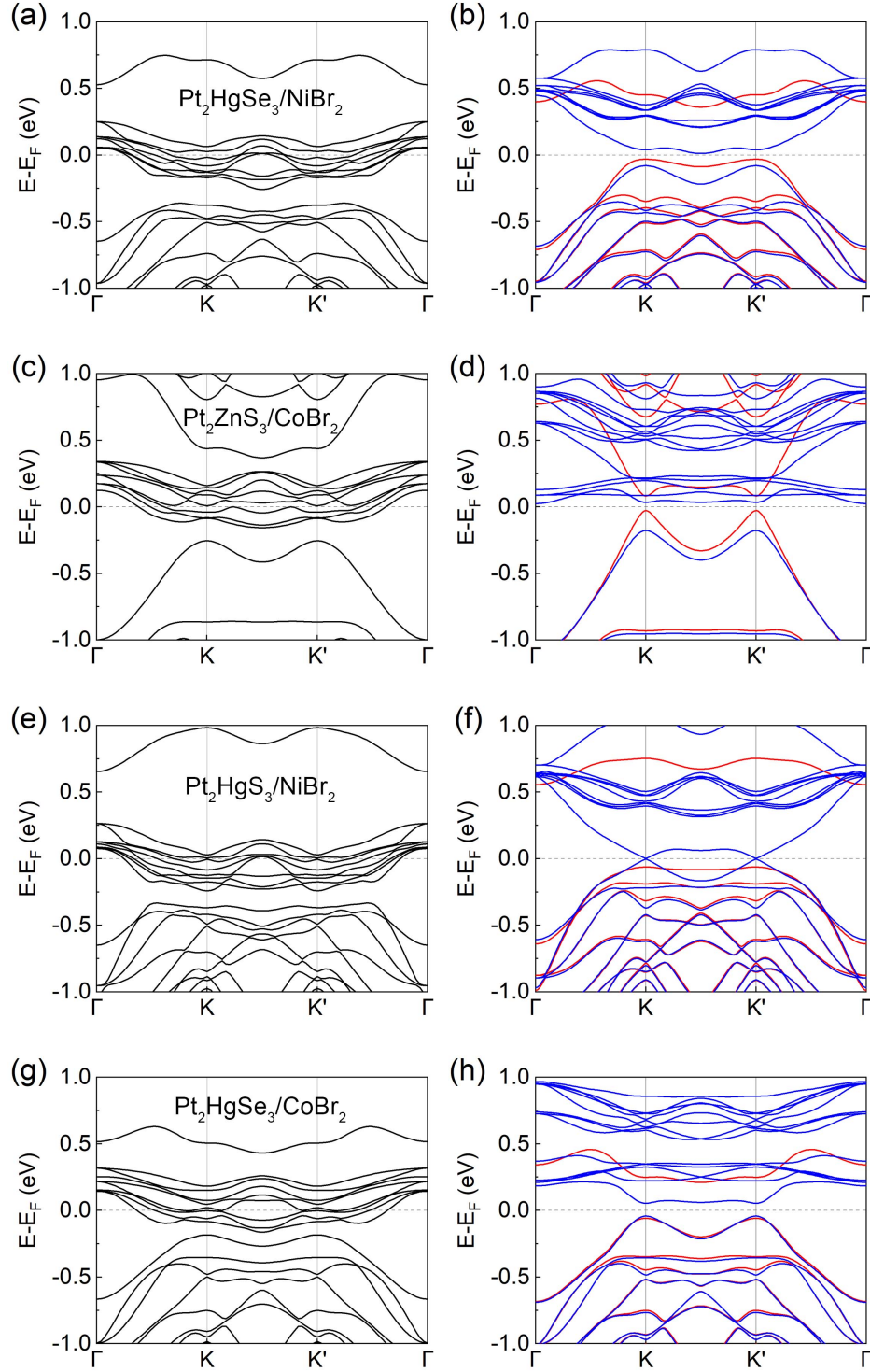
13

FIG. S8. Band structures of (a)-(b) $Pt_2HgSe_3/NiBr_2$, (c)-(d) $Pt_2ZnS_3/CoBr_2$, (e)-(f) $Pt_2HgS_3/NiBr_2$, and (g)-(h) $Pt_2HgSe_3/CoBr_2$ without and with magnetization. Left column shows band structures without magnetization. Right column shows the spin-polarized band structures with magnetization and the red (blue) color denotes spin up (down) state.

14

VII. STRAIN EFFECT OF INTERLAYER DISTANCE ON GLOBAL BAND GAPS

We calculate the total energies and the band structures of $Pt_2HgSe_3/NiBr_2$, $Pt_2ZnS_3/CoBr_2$, $Pt_2HgS_3/NiBr_2$, and $Pt_2HgSe_3/CoBr_2$ with different interlayer distance d (vdW gap). In our calculation, the interlayer distance d is changed from -10 % to 10 % compared to the initial structure. After the optimization with magnetization and Hubbard U, the total energies and the global band gaps are plotted in S9. We find the $Pt_2ZnS_3/CoBr_2$ becomes metallic with tensile strain over 6 % [so there is no data at tensile strain of 6 %, 8 %, and 10 %, see Fig. S9(b)] and the band gap becomes trivial with the vdW gap strain below 2 %. The total energy calculations show that the initial structure without strain is the most stable state in $Pt_2HgSe_3/NiBr_2$, $Pt_2HgS_3/NiBr_2$, and $Pt_2HgSe_3/CoBr_2$. For $Pt_2HgS_3/NiBr_2$ and $Pt_2ZnS_3/CoBr_2$, as displayed in Figs. S9(a) and S9(b), we find that the reducing interlayer distance enhances the global band gap. However, the band gaps of $Pt_2HgS_3/NiBr_2$ and $Pt_2HgSe_3/CoBr_2$ exhibit the maximum with the vdW gap strain around -2 % to 0 % [see Figs. S9(c) and S9(d)].
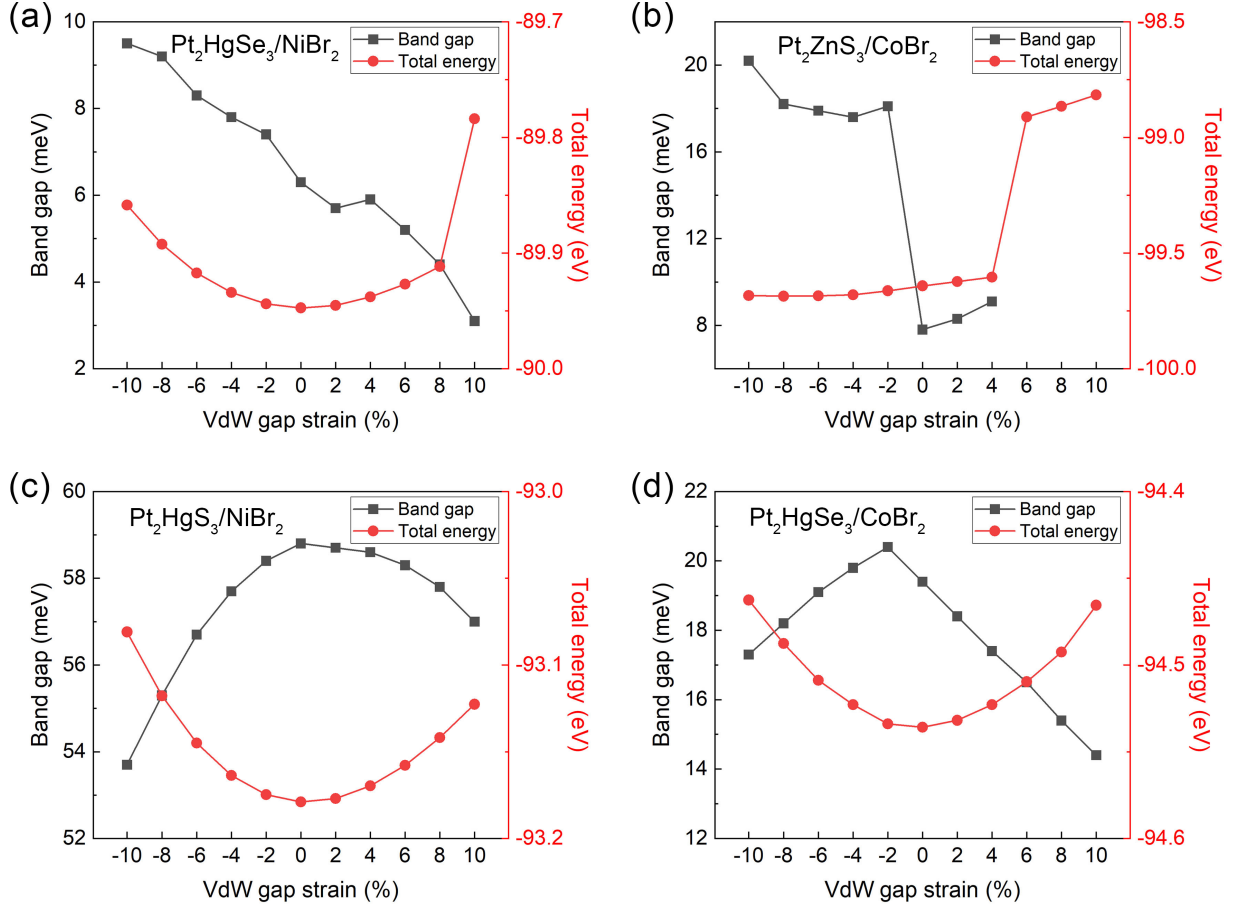
FIG. S9. Global band gap (black) and the total energy (red) of (a) $Pt_2HgSe_3/NiBr_2$, (b) $Pt_2ZnS_3/CoBr_2$, (c) $Pt_2HgS_3/NiBr_2$, and (d) $Pt_2HgSe_3/CoBr_2$ as a function vdW gap with compressive/tensile strain from -10.0 % to 10.0 %.

VIII. CHARGE DENSITY DIFFERENCE AND PLANAR-AVERAGED POTENTIAL FOR 8 KINDS OF TYPICAL PT$_2AX_3/MY_2$ HETEROSTRUCTURES

To investigate and analyze the interfacial characteristics, we carried out the charge density difference and planar-averaged electrostatic potential as shown in Fig.S10 and Fig.S11. One can notice that the charge density redistributes at the interface, leading to a built-in electric field and an enhancement of Rashba SOC.
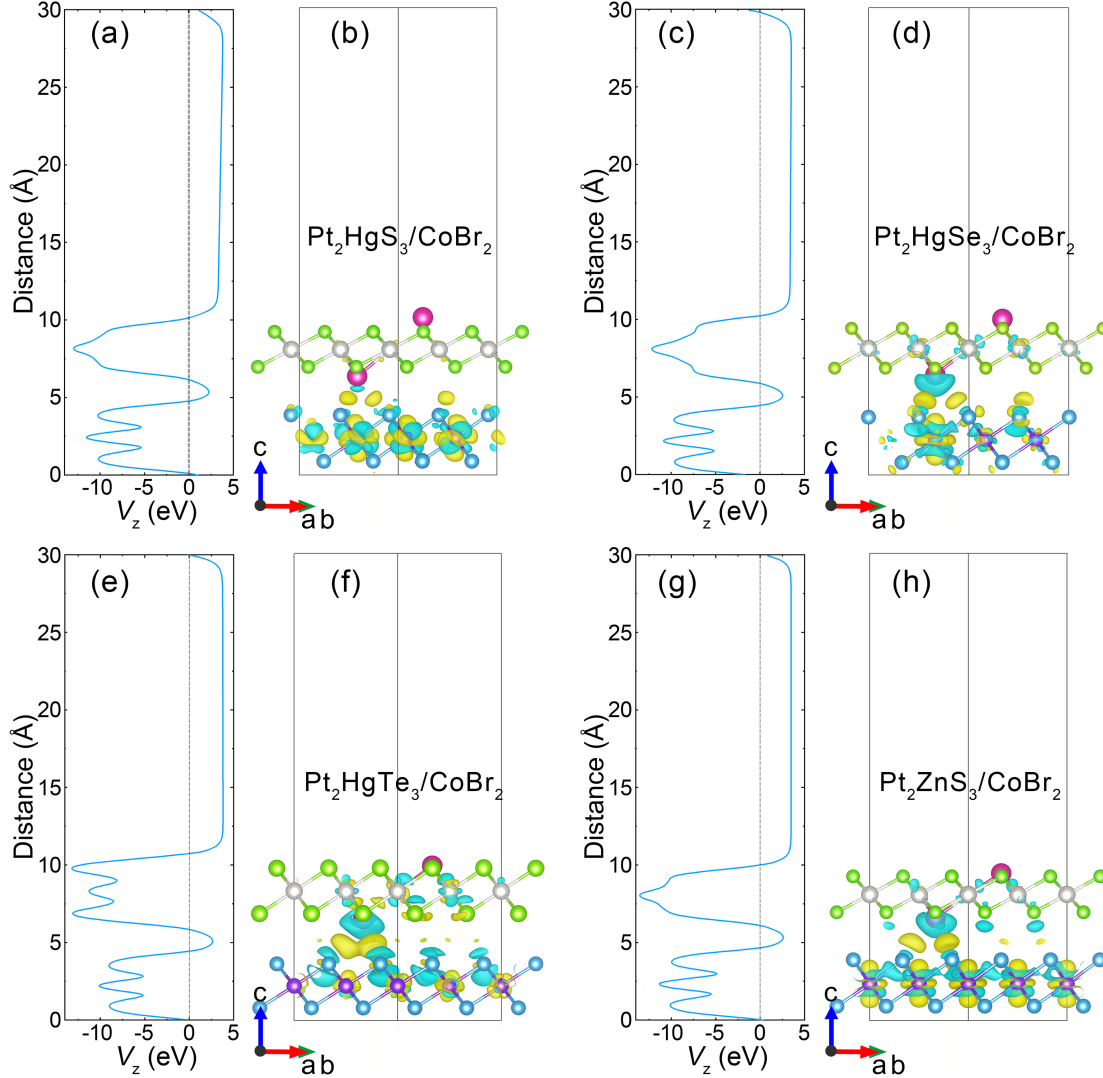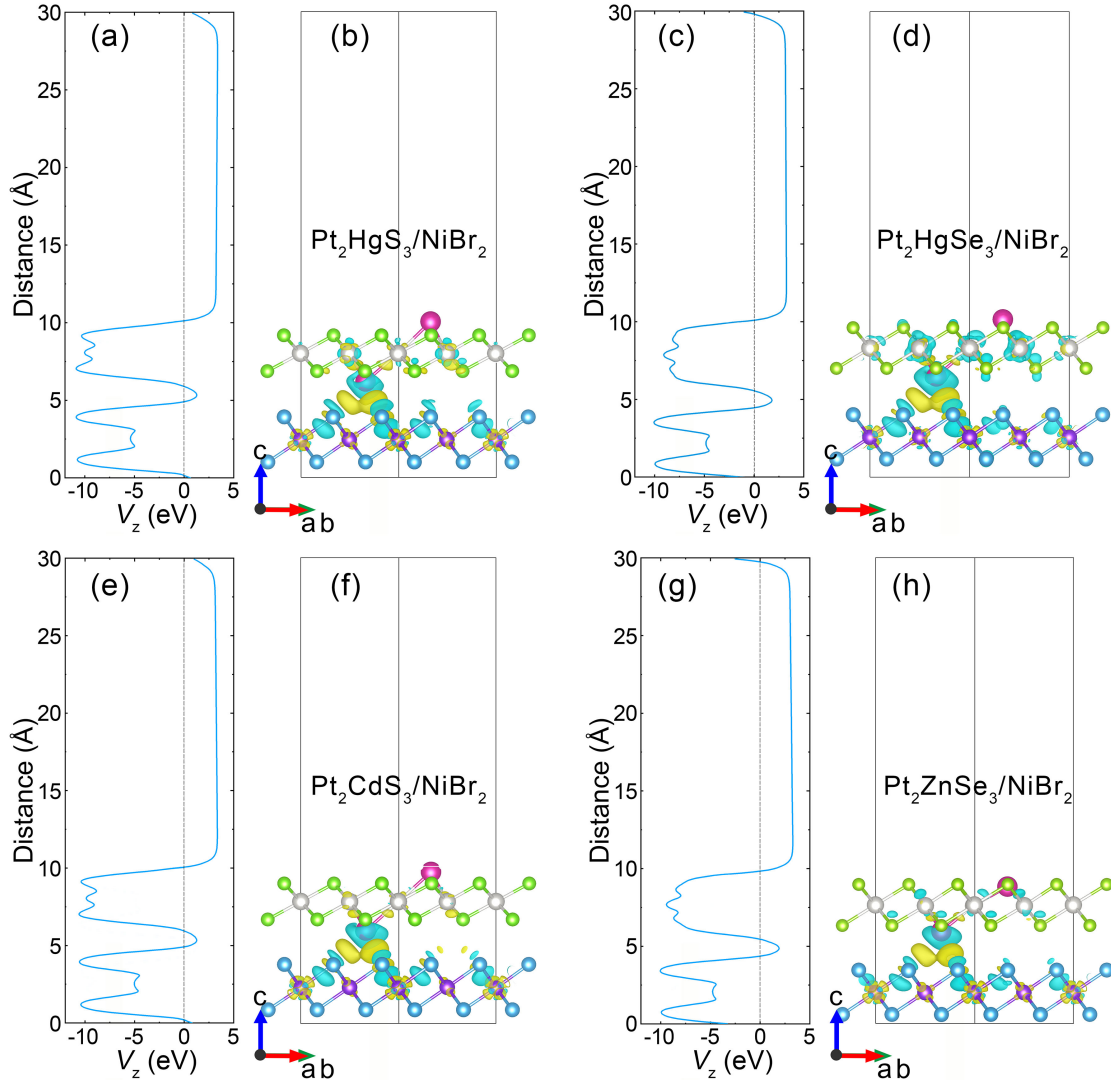

FIG. S10. The planar-averaged electrostatic potential along z direction and charge density difference of vdW heterostructures constructed as (a)-(b) Pt$_2$HgS$_3$/CoBr$_2$, (c)-(d) Pt$_2$HgSe$_3$/CoBr$_2$, (e)-(f) Pt$_2$HgTe$_3$/CoBr$_2$, (g)-(h) Pt$_2$ZnS$_3$/CoBr$_2$. Cyan and yellow contours represent charge loss and accumulation, respectively.

FIG. S11. The planar-averaged electrostatic potential along z direction and charge density difference of vdW heterostructures constructed as (a)-(b) Pt$_2$HgS$_3$/NiBr$_2$, (c)-(d) Pt$_2$HgSe$_3$/NiBr$_2$, (e)-(f) Pt$_2$CdS$_3$/NiBr$_2$, (g)-(h) Pt$_2$ZnSe$_3$/NiBr$_2$. Cyan and yellow contours represent charge loss and accumulation, respectively.

18

IX. BAND STRUCTURES AND VALLEY SPLITTINGS OF 44 KINDS OF WELL-MATCHED VDW HETEROSTRUCTURES

Figures S12-S23 display the band structures without SOC, with SOC, and with layer projection for 44 kinds of well-matched systems as listed in Table S5. We specified them into nine groups corresponding to the Pt_2AX_3 family, i.e., Pt_2CdS_3 (see Fig. S12), Pt_2CdSe_3 (see Fig. S13), Pt_2CdTe_3 (see Fig. S14), Pt_2HgS_3 (see Figs. S15 and S16), Pt_2HgSe_3 (see Figs. S17 and S18), Pt_2HgTe_3 (see Fig. S19), Pt_2ZnS_3 (see Figs. S20 and S21), Pt_2ZnSe_3 (see Fig. S22), and Pt_2ZnTe_3 (see Fig. S23), respectively.

From the spin-resolved band structures without SOC as displayed in Figs. S12-S23, one can find that magnetic substrates induces sizable Zeeman splitting of the spin up/down bands. When SOC is considered, valley polarization can be universally observed in these systems, which is originated from the breaking of inversion symmetry and time-reversal symmetry. Layer-resolved band structures show that the electronic states near the Fermi level are mainly dominated by the topological Pt_2AX_3 layer, indicating the electronic structures of the Pt_2AX_3 monolayer are modified by the proximity effect. We summarized all stacking configurations, valley splittings, and global band gaps of these well-matched systems in Table S5.

TABLE S5. Stacking configuration, valley splitting Δ (meV), and global band gap E_g (meV) of 44 kinds of well-matched vdW heterostructures.

Well-matched system	Stack	Δ	E_g	Well-matched system	Stack	Δ	E_g
$Pt_2CdS_3/CoBr_2$[a]	i	-79.8	/[b]	$Pt_2HgSe_3/FeBr_2$	iii	86.7	/
$Pt_2CdS_3/CoCl_2$	iii	-50.4	/	$Pt_2HgSe_3/FeCl_2$	ii	42.3	/
$Pt_2CdS_3/FeBr_2$	iii	-55.6	/	$Pt_2HgSe_3/MnBi_2Te_4$	iv	0.9	/
$Pt_2CdS_3/FeCl_2$	iii	-48.4	/	$Pt_2HgSe_3/NiBr_2$	i	134.2	6.3
$Pt_2CdS_3/NiBr_2$	i	85.3	/	Pt_2HgSe_3/VI_3 (1×1)	iv	0.3	
Pt_2CdS_3/VI_3 (1×1)	iii	0.1	/	$Pt_2HgTe_3/CoBr_2$	i	5	14.7
$Pt_2CdSe_3/FeBr_2$	ii	-22.1	/	$Pt_2HgTe_3/FeBr_2$	i	6.7	/
$Pt_2CdSe_3/FeCl_2$	iii	3	/	Pt_2HgTe_3/FeI_2	iii	-24.2	/
$Pt_2CdSe_3/NiBr_2$	i	41.2	/	$Pt_2HgTe_3/MnBi_2Te_4$	iv	0.1	/
Pt_2CdSe_3/VI_3 (1×1)	iv	-0.3	/	Pt_2HgTe_3/NiI_2	i	-43.2	/
$Pt_2CdTe_3/FeBr_2$	i	-52.2	/	$Pt_2ZnS_3/CoBr_2$	i	36.3	7.8
$Pt_2HgS_3/CoBr_2$	iii	-15.3	145.3	$Pt_2ZnS_3/FeBr_2$	iii	33.5	/
$Pt_2HgS_3/CoCl_2$	iii	-14.8	65.8	$Pt_2ZnS_3/FeCl_2$	ii	-27.1	/
Pt_2HgS_3/CrI_3 (1×1)	iv	7.2	39.1	Pt_2ZnS_3/FeI_2 $(\sqrt{3} \times \sqrt{3})$	i	-17.3	/
$Pt_2HgS_3/FeBr_2$	iii	-11.1	195.5	$Pt_2ZnS_3/NiCl_2$	i	-133.8	/
$Pt_2HgS_3/FeCl_2$	iii	-8.4	/	Pt_2ZnS_3/NiI_2 $(\sqrt{3} \times \sqrt{3})$	iv	75.3	/
Pt_2HgS_3/FeI_2 $(\sqrt{3} \times \sqrt{3})$	i	-15.6	105.2	Pt_2ZnS_3/VI_3 (1×1)	iii	0.3	/
$Pt_2HgS_3/NiBr_2$	i	15.4	58.8	$Pt_2ZnSe_3/FeBr_2$	iii	13.6	/
Pt_2HgS_3/NiI_2 $(\sqrt{3} \times \sqrt{3})$	iv	-47.1	38.7	$Pt_2ZnSe_3/FeCl_2$	iii	7.9	/
Pt_2HgS_3/VI_3 (1×1)	iv	22	/	$Pt_2ZnSe_3/NiBr_2$	i	-80.6	/
$Pt_2HgSe_3/CoBr_2$	iii	3.5	19.3	$Pt_2ZnTe_3/FeBr_2$	iii	-24.6	/
$Pt_2HgSe_3/CoCl_2$	i	-6.1	0.9	Pt_2ZnTe_3/FeI_2	i	-128.2	/

[a] The supercell size of the substrate is 2×2 by default except $MnBi_2Te_4$ with $\sqrt{3} \times \sqrt{3}$ supercell.
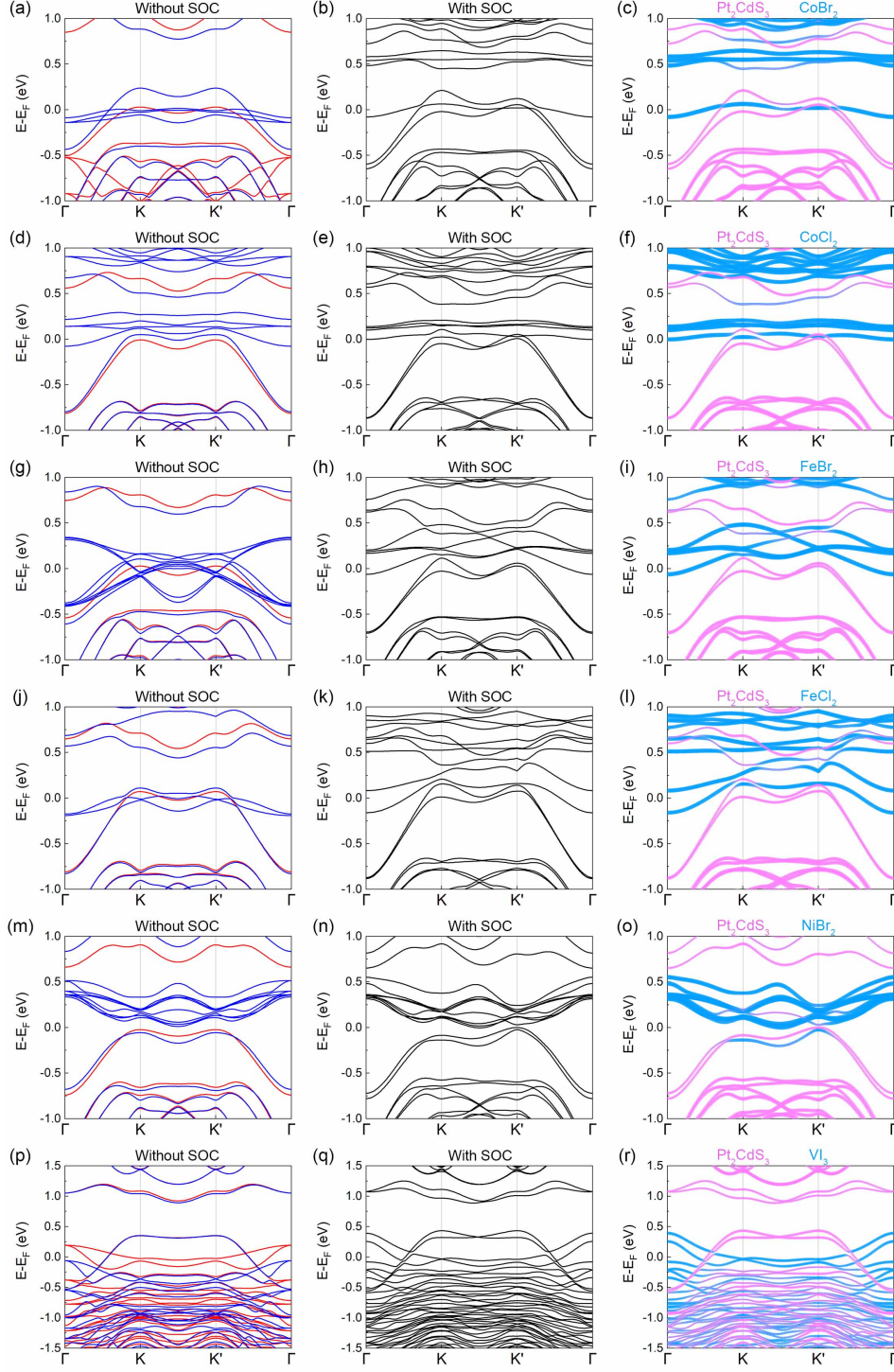[b] "/" denotes that the system does not have a global band gap, i.e., the system is metallic.

FIG. S12. Band structures of 6 well-matched heterostructures based on monolayer Pt_2CdS_3. Left column shows the spin-resolved band structures without SOC and the red (blue) color denotes spin up (down) state. Right column shows the layer-resolved band structures with SOC. The pink bubble represents the element projection of jacutingaite family layer whereas the light blue bubble represents the element projection of ferromagnetic substrate layer.
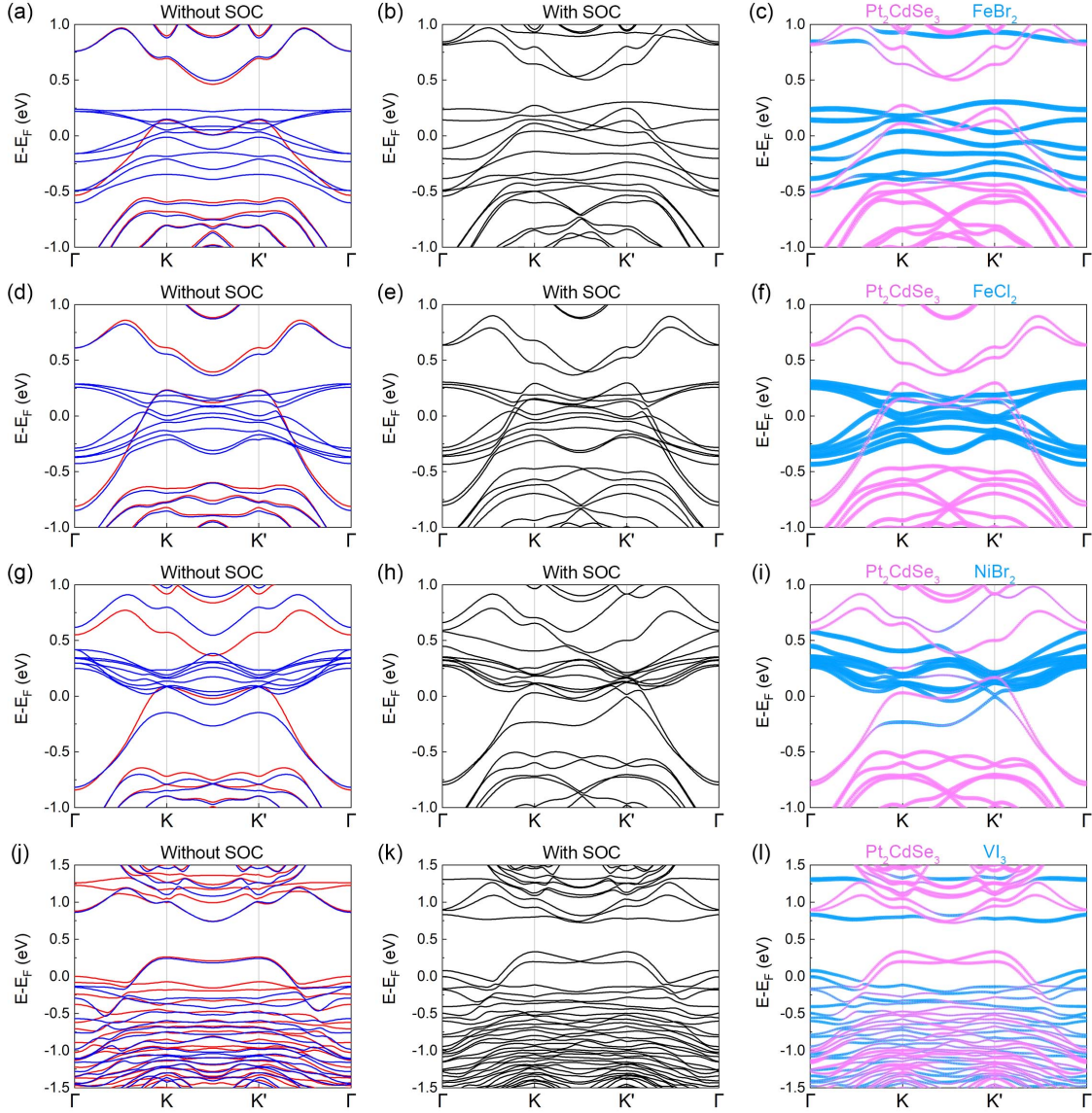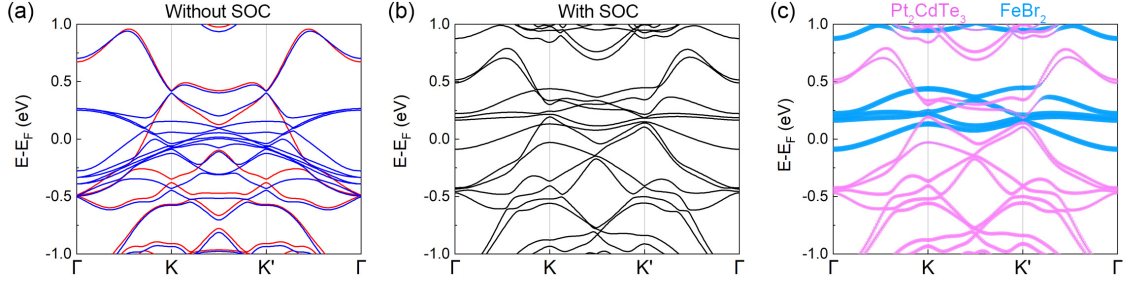
21

FIG. S13. Band structures of 4 well-matched heterostructures based on monolayer Pt_2CdSe_3. Left column shows the spin-resolved band structures without SOC and the red (blue) color denotes spin up (down) state. Right column shows the layer-resolved band structures with SOC. The pink bubble represents the element projection of jacutingaite family layer whereas the light blue bubble represents the element projection of ferromagnetic substrate layer.
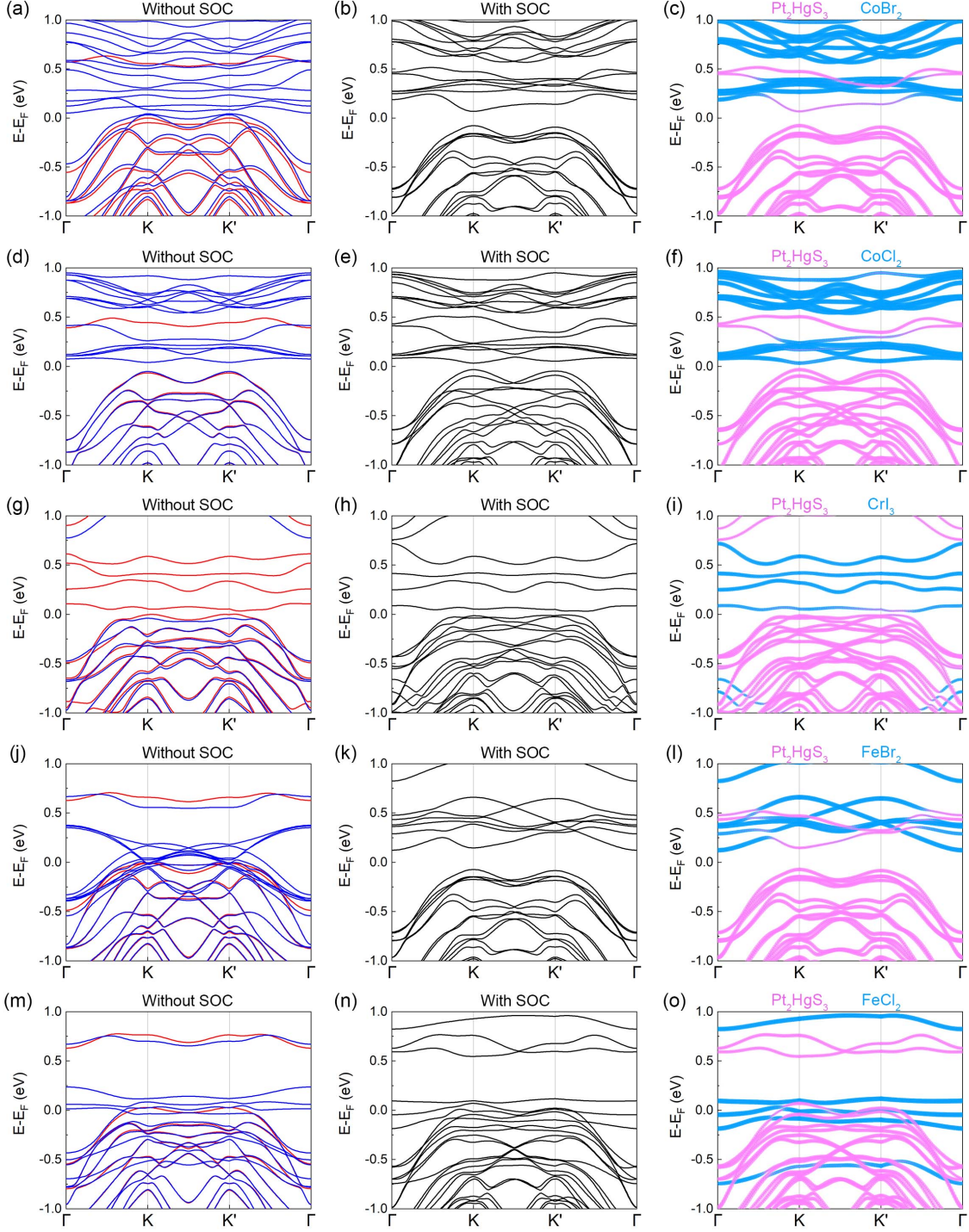
FIG. S14. Band structures of one well-matched heterostructure based on monolayer Pt_2CdTe_3. Figure (a) shows the spin-resolved band structures without SOC and the red (blue) color denotes spin up (down) state. Figure (c) shows the layer-resolved band structures with SOC. The pink bubble represents the element projection of jacutingaite family layer whereas the light blue bubble represents the element projection of ferromagnetic substrate layer.
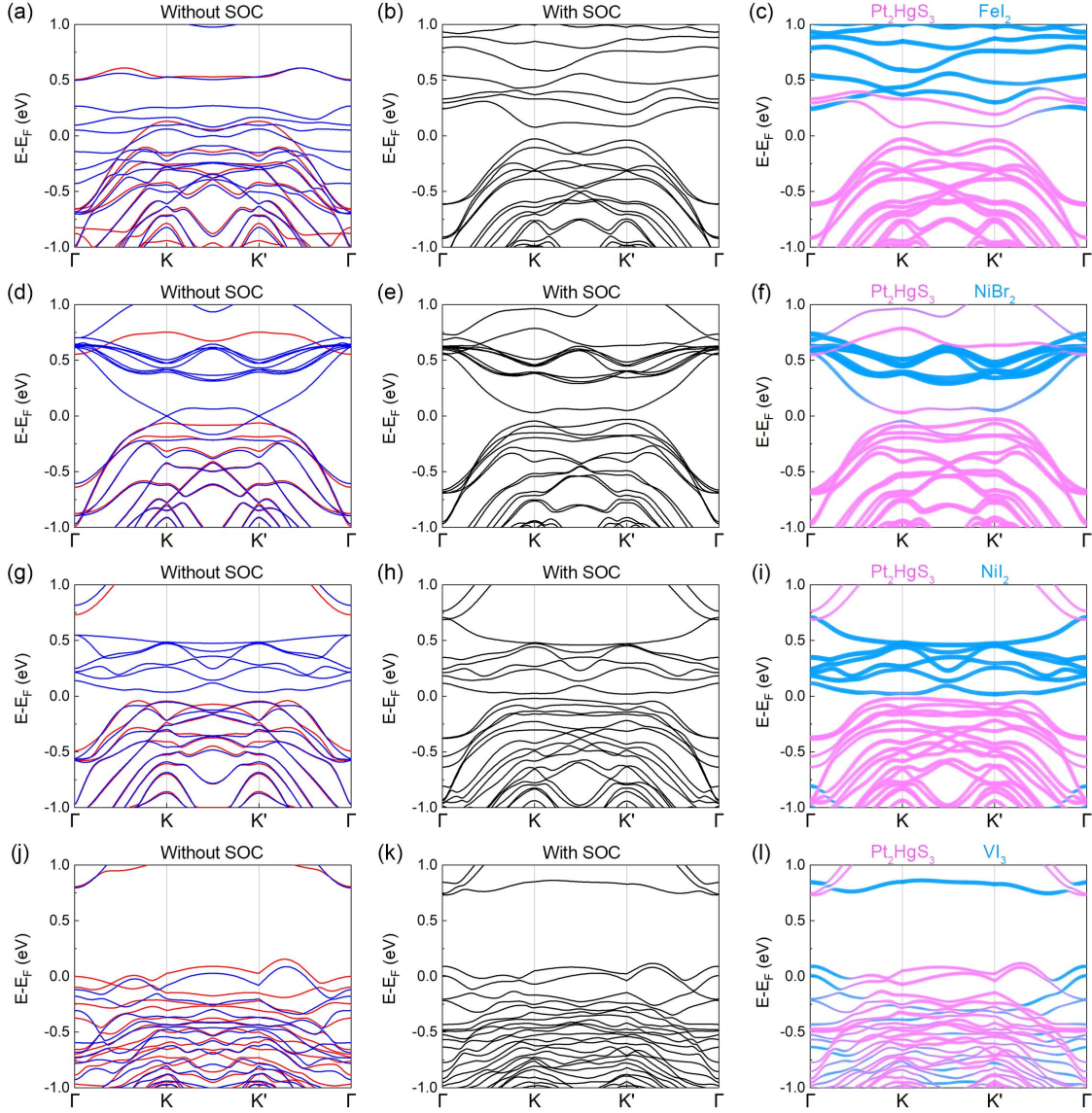
FIG. S15. Band structures of 5 in 9 well-matched heterostructures based on monolayer Pt_2HgS_3. Left column shows the spin-resolved band structures without SOC and the red (blue) color denotes spin up (down) state. Right column shows the layer-resolved band structures with SOC. The pink bubble represents the element projection of jacutingaite family layer whereas the light blue bubble represents the element projection of ferromagnetic substrate layer.
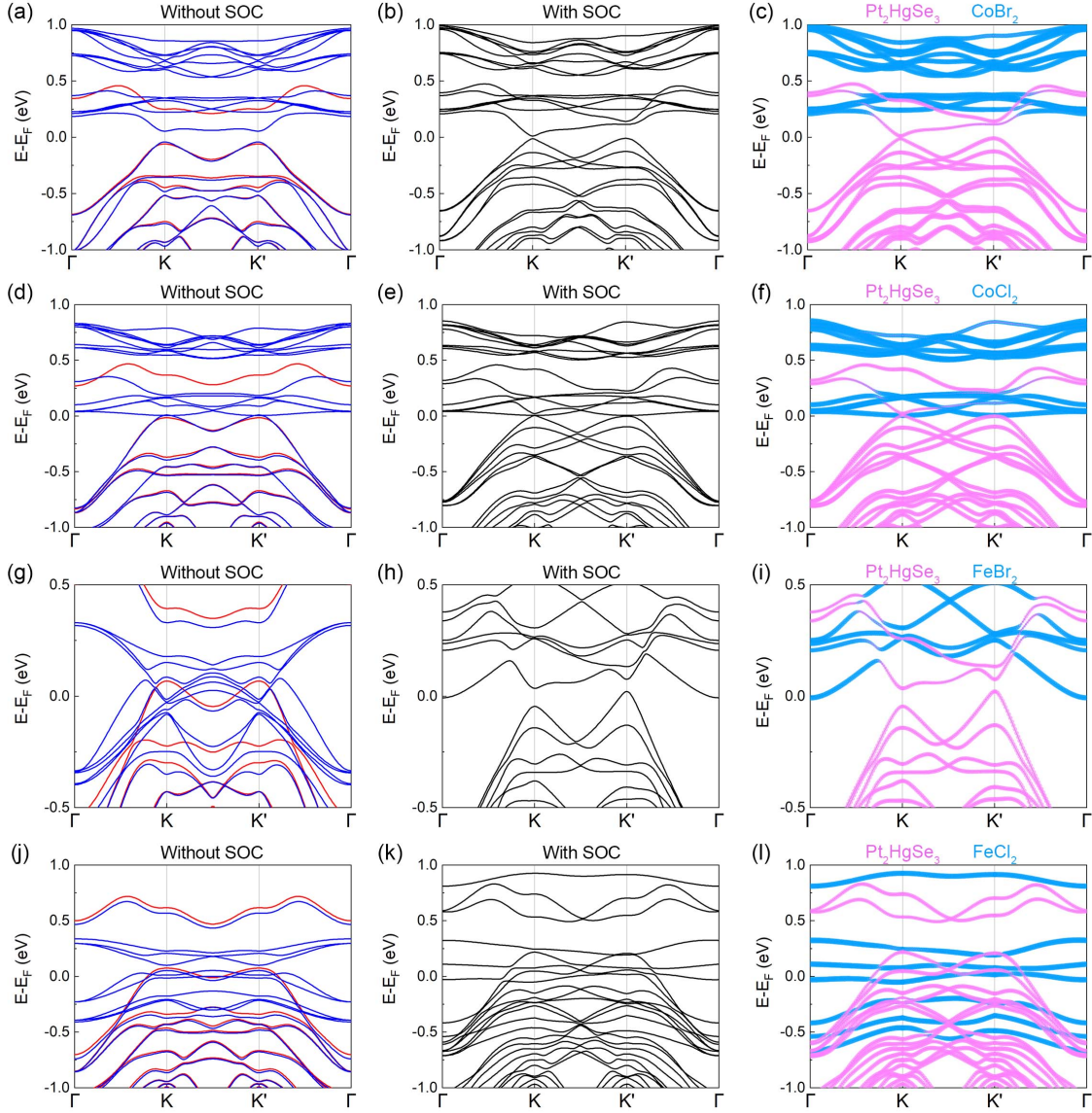
FIG. S16. Band structures of other 4 in 9 well-matched heterostructures based on monolayer Pt_2HgS_3. Left column shows the spin-resolved band structures without SOC and the red (blue) color denotes spin up (down) state. Right column shows the layer-resolved band structures with SOC. The pink bubble represents the element projection of jacutingaite family layer whereas the light blue bubble represents the element projection of ferromagnetic substrate layer.

FIG. S17. Band structures of 4 in 7 well-matched heterostructures based on monolayer Pt_2HgSe_3. Left column shows the spin-resolved band structures without SOC and the red (blue) color denotes spin up (down) state. Right column shows the layer-resolved band structures with SOC. The pink bubble represents the element projection of jacutingaite family layer whereas the light blue bubble represents the element projection of ferromagnetic substrate layer.
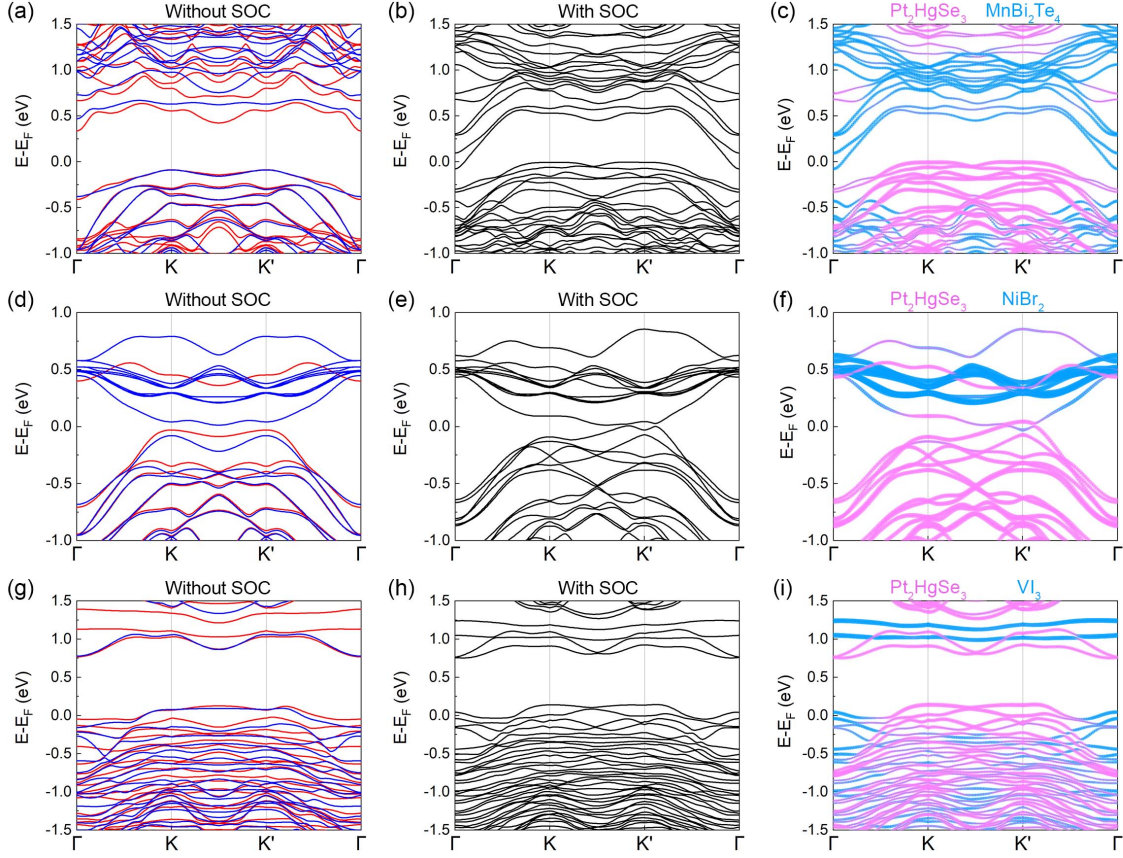
FIG. S18. Band structures of other 3 in 7 well-matched heterostructures based on monolayer Pt$_2$HgSe$_3$. Left column shows the spin-resolved band structures without SOC and the red (blue) color denotes spin up (down) state. Right column shows the layer-resolved band structures with SOC. The pink bubble represents the element projection of jacutingaite family layer whereas the light blue bubble represents the element projection of ferromagnetic substrate layer.
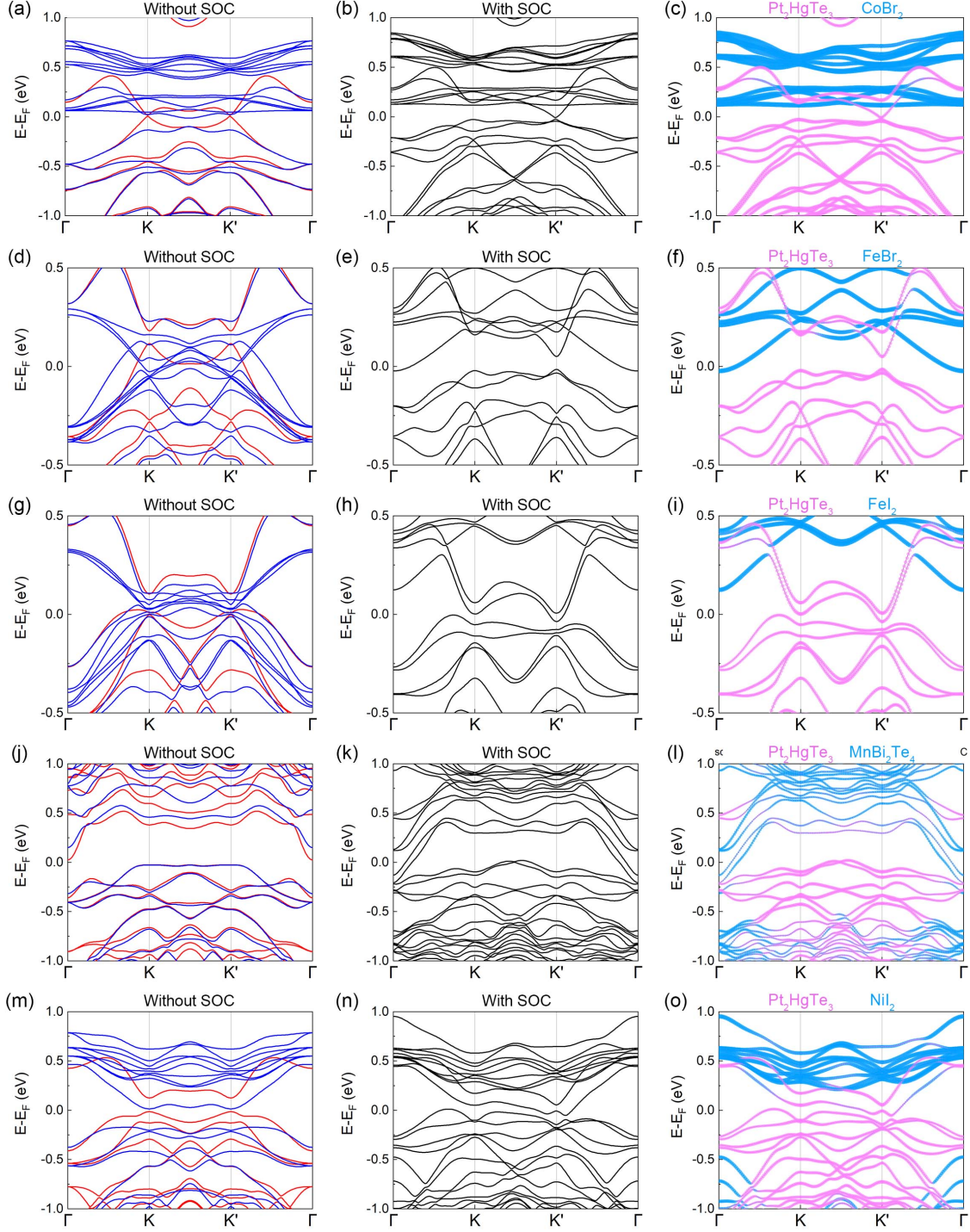
FIG. S19. Band structures of 5 well-matched heterostructures based on monolayer Pt_2HgTe_3. Left column shows the spin-resolved band structures without SOC and the red (blue) color denotes spin up (down) state. Right column shows the layer-resolved band structures with SOC. The pink bubble represents the element projection of jacutingaite family layer whereas the light blue bubble represents the element projection of ferromagnetic substrate layer.
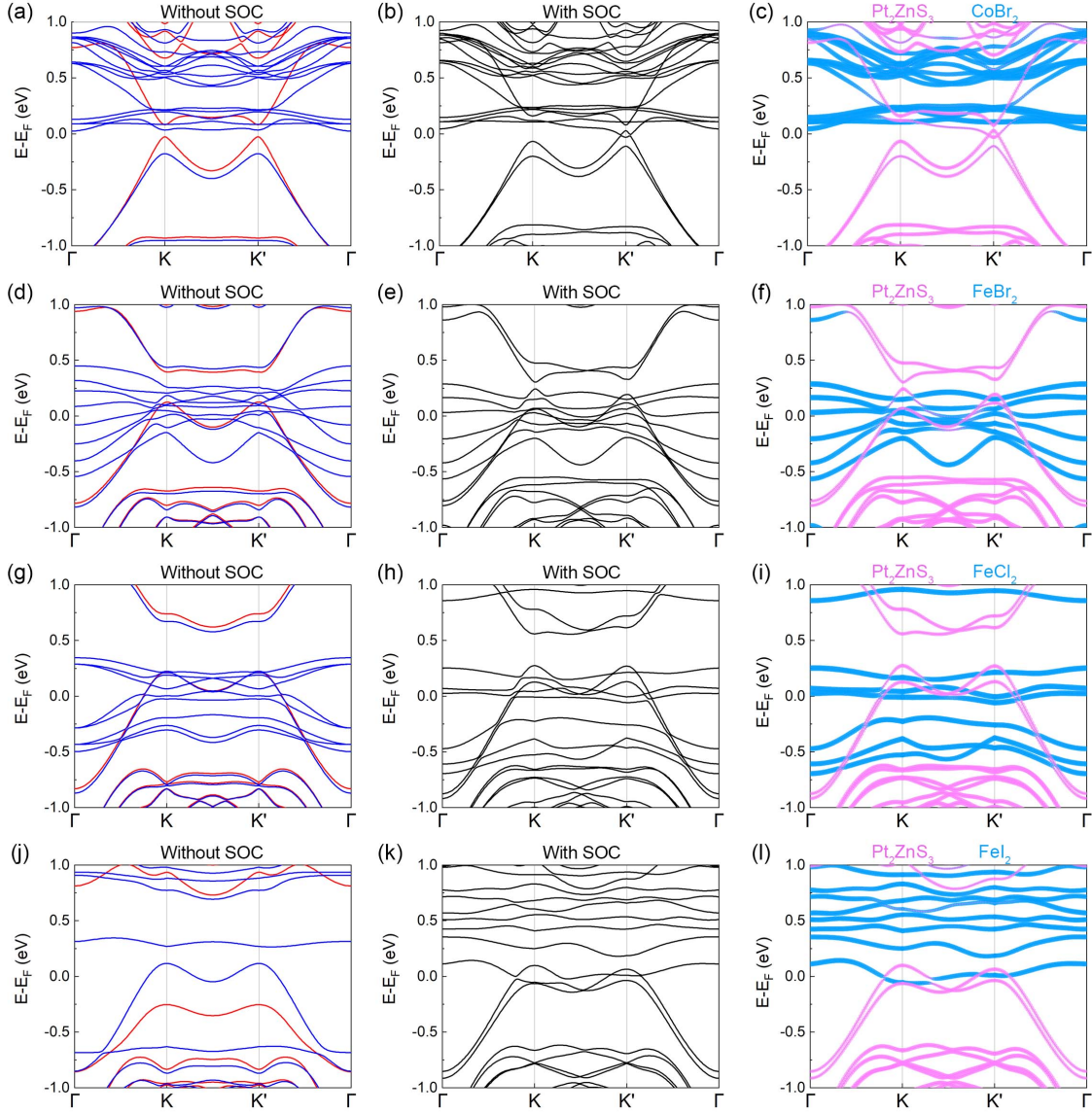
28

FIG. S20. Band structures of 4 in 7 well-matched heterostructures based on monolayer Pt_2ZnS_3. Left column shows the spin-resolved band structures without SOC and the red (blue) color denotes spin up (down) state. Right column shows the layer-resolved band structures with SOC. The pink bubble represents the element projection of jacutingaite family layer whereas the light blue bubble represents the element projection of ferromagnetic substrate layer.
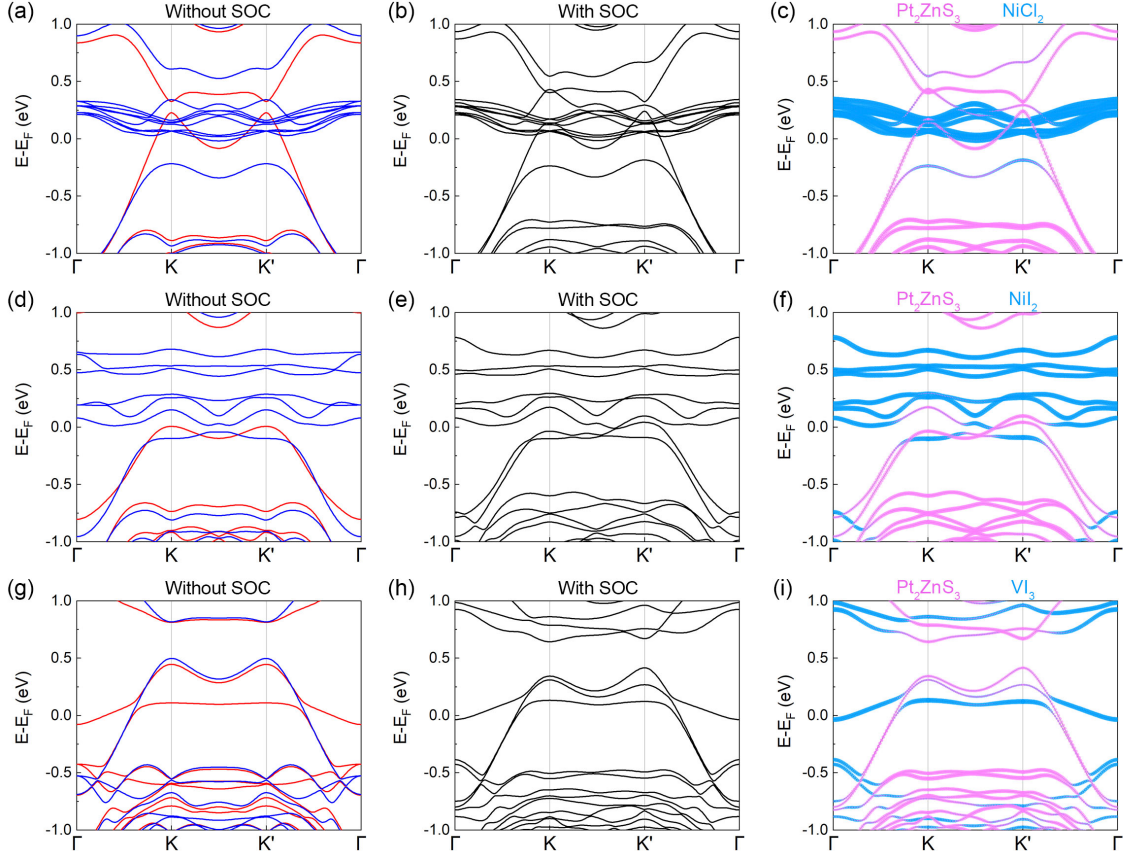
FIG. S21. Band structures of other 3 in 7 well-matched heterostructures based on monolayer Pt_2ZnS_3. Left column shows the spin-resolved band structures without SOC and the red (blue) color denotes spin up (down) state. Right column shows the layer-resolved band structures with SOC. The pink bubble represents the element projection of jacutingaite family layer whereas the light blue bubble represents the element projection of ferromagnetic substrate layer.

FIG. S22. Band structures of three well-matched heterostructures based on monolayer Pt_2ZnSe_3. Left column shows the spin-resolved band structures without SOC and the red (blue) color denotes spin up (down) state. Right column shows the layer-resolved band structures with SOC. The pink bubble represents the element projection of jacutingaite family layer whereas the light blue bubble represents the element projection of ferromagnetic substrate layer.
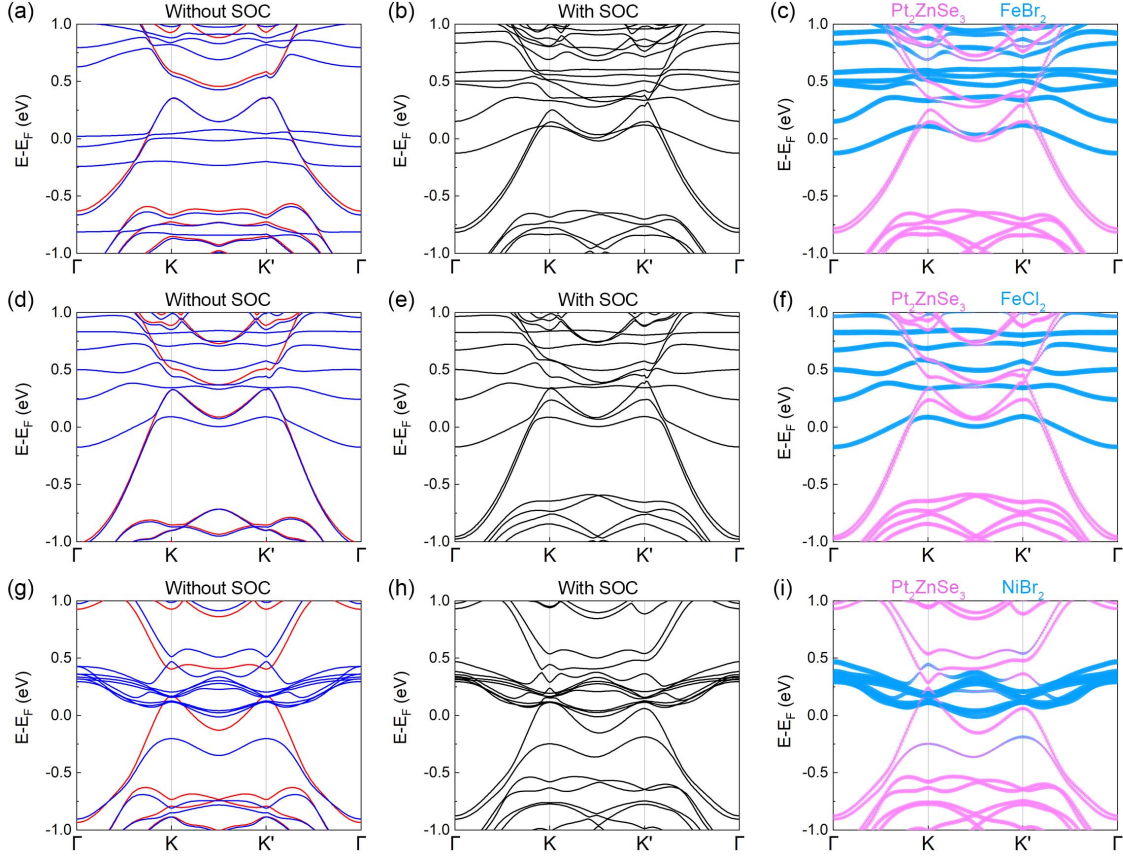
FIG. S23. Band structures of two well-matched heterostructures based on monolayer Pt_2ZnTe_3. Left column shows the spin-resolved band structures without SOC and the red (blue) color denotes spin up (down) state. Right column shows the layer-resolved band structures with SOC. The pink bubble represents the element projection of jacutingaite family layer whereas the light blue bubble represents the element projection of ferromagnetic substrate layer.
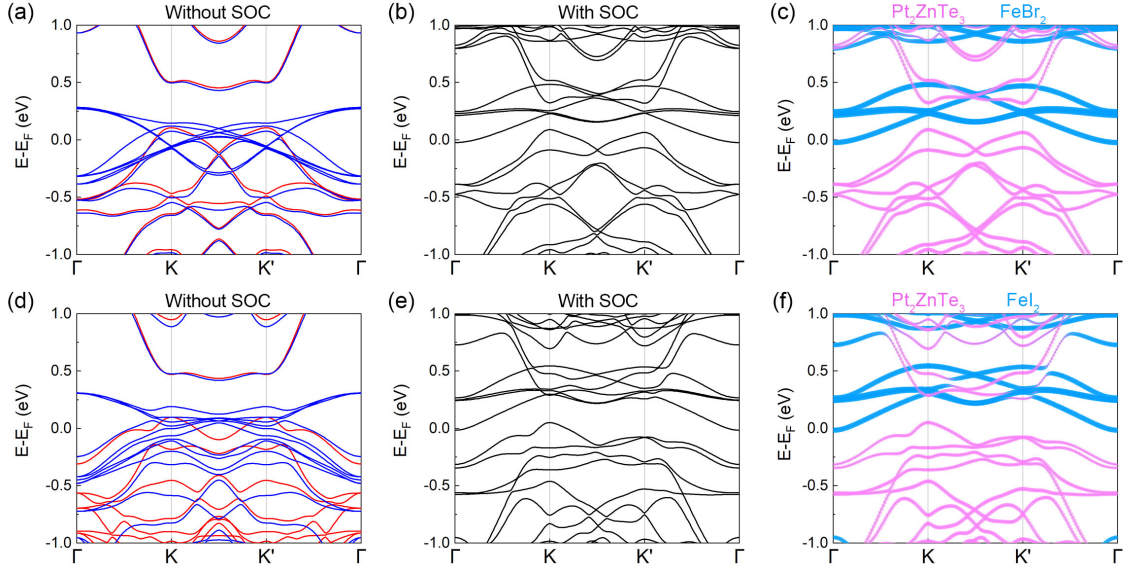
[1] P. E. Blöchl, Phys. Rev. B **50**, 17953 (1994).

[2] G. Kresse and J. Furthmuller, Phys. Rev. B **54**, 11169 (1996).

[3] G. Kresse and D. Joubert, Phys. Rev. B **59**, 1758 (1999).

[4] J. P. Perdew, J. A. Chevary, S. H. Vosko, K. A. Jackson, M. R. Pederson, D. J. Singh, and C. Fiolhais, Phys. Rev. B **46**, 6671 (1992).

[5] S. Grimme, J. Antony, S. Ehrlich, and H. Krieg, J. Chem. Phys. **132**, 154104 (2010).

[6] H. J. Kulik, M. Cococcioni, D. A. Scherlis, and N. Marzari, Phys. Rev. Lett. **97**, 103001 (2006).

[7] V. V. Kulish and W. Huang, J. Mater. Chem. C **5**, 8734 (2017).

[8] B. Huang, G. Clark, E. N.-Moratalla, D. R. Klein, R. Cheng, K. L. Seyler, D. Zhong, E. Schmidgall, M. A. McGuire, D. H. Cobden, W. Yao, Di Xiao, P. J.-Herrero and X. Xu, Nature (London) **546**, 270 (2017).

[9] D. Zhong, K. L. Seyler, X. Linpeng, R. Cheng, N. Sivadas, B. Huang, E. Schmidgall, T. Taniguchi, K. Watanabe, M. A. McGuire, W. Yao, D. Xiao, K.-M. C. Fu, and X. Xu, Sci. Adv. **3**, e1603113 (2017).

[10] M. M. Otrokov, I. P. Rusinov, M. Blanco-Rey, M. Hoffmann, A. Yu. Vyazovskaya, S. V. Eremeev, A. Ernst, P. M. Echenique, A. Arnau, and E. V. Chulkov, Phys. Rev. Lett. **122**, 107202 (2019).

[11] M. A. McGuire, Crystals **7**, 121 (2017).

[12] V. V. Kulish and W. Huang, J. Mater. Chem. C **5**, 8734 (2017).

[13] B. Huang, G. Clark, E. N.-Moratalla, D. R. Klein, R. Cheng, K. L. Seyler, D. Zhong, E. Schmidgall, M. A. McGuire, D. H. Cobden, W. Yao, Di Xiao, P. J.-Herrero and X. Xu, Nature (London) **546**, 270 (2017).

[14] M. M. Otrokov, I. P. Rusinov, M. Blanco-Rey, M. Hoffmann, A. Yu. Vyazovskaya, S. V. Eremeev, A. Ernst, P. M. Echenique, A. Arnau, and E. V. Chulkov, Phys. Rev. Lett. **122**, 107202 (2019).

[15] S. Tian, J.-F. Zhang, C. Li, T. Ying, S. Li, X. Zhang, K. Liu, and H. Lei, J. Am. Chem. Soc. **141**, 5326 (2019).

[16] H. Y. Lv, W. J. Lu, X. Luo, X. B. Zhu, and Y. P. Sun, Phys. Rev. B **99**, 134416 (2019).

[17] A. S. Botana, and M. R. Norman, Phys. Rev. Mater. **3**, 044001 (2019).

[18] M. M. Otrokov, I. P. Rusinov, M. Blanco-Rey, M. Hoffmann, A. Yu. Vyazovskaya, S. V. Eremeev, A. Ernst, P. M. Echenique, A. Arnau, and E. V. Chulkov, Phys. Rev. Lett. **122**, 107202 (2019).

[19] X. Li, Z. Zhang, and H. Zhang, Nanoscale Adv. **2**, 495 (2020).

[20] M. Lu, Q. Yao, C. Xiao, C. Huang, and E. Kan, ACS Omega **4**, 5714 (2019).

[21] D. Zhong, K. L. Seyler, X. Linpeng, R. Cheng, N. Sivadas, B. Huang, E. Schmidgall, T. Taniguchi, K. Watanabe, M. A. McGuire, W. Yao, D. Xiao, K.-M. C. Fu, and X. Xu, Sci. Adv. **3**, e1603113 (2017).

[22] L. Webster and J.-A. Yan, Phys. Rev. B **98**, 144411 (2018).

[23] C. Gong, L. Li, Z. Li, H. Ji, A. Stern, Y. Xia, T. Cao, W. Bao, C. Wang, Y. Wang, Z. Q. Qiu, R. J. Cava, S. G. Louie, J. Xia, and X. Zhang, Nature (London) **546**, 265 (2017).

[24] S. Jiang, J. Shan, and K. F. Mak, Nat. Mater. **17**, 406 (2018).

[25] K. F. Mak, J. Shan, and D. C. Ralph, Nat. Rev. Phys. **1**, 646 (2019).

[26] W. Zhuo, B. Lei, S. Wu, F. Yu, C. Zhu, J. Cui, Z. Sun, D. Ma, M. Shi, H. Wang, W. Wang, T. Wu, J. Ying, S. Wu, Z. Wang, and X. Chen, Adv. Mater. **33**, 2008586 (2021).

[27] A. A. Mostofi, J. R. Yates, Y. S. Lee, I. Souza, D. Vanderbilt, and N. Marzari, Comput. Phys. Commun. **178**, 685 (2008).

[28] G. Pizzi, V. Vitale, R. Arita, S. Blugel, F. Freimuth, G.Geranton, M. Gibertini, D. Gresch, C. Johnson, T. Koretsune *et al.*, J. Phys. Condens. Matter **32**, 165902 (2020).

[29] Q. S. Wu, S. N. Zhang, H.-F. Song, M. Troyer, and A. A. Soluyanov, Comput. Phys. Commun. **224**, 405 (2018).